Supramolecular organization and dynamics of mannosylated phosphatidylinositol lipids in the mycobacterial plasma membrane

Chelsea Brown, Robin Corey, Axelle Grélard, Ya Gao, Yeol Kyo Choi, Emanuel Luna, Martine Gilleron, Nicolas Destainville, Jérôme Nigou, Antoine Loquet, et al.

Supramolecular Organisation and Dynamics of Mannosylated Phosphatidylinositol Lipids in the Mycobacterial Plasma Membrane

Chelsea M. Brown[1], Robin A. Corey[2], Axelle Grélard[3], Ya Gao[4,5], Yeol Kyo Choi[5], Emanuel Luna[5], Martine Gilleron[6], Nicolas Destainville[7], Jérôme Nigou[6], Antoine Loquet[3], Elizabeth Fullam[1], Wonpil Im[5,], Phillip J. Stansfeld[1,8,*,+], Matthieu Chavent[6,*,+]*

[1] School of Life Sciences,
University of Warwick,
Coventry,
CV4 7AL,
UK

[2] Department of Biochemistry,
University of Oxford,
Oxford,
UK

[3] Université de Bordeaux,
CBMN (UMR5248),
CNRS, IPB,
Institut Européen de Chimie et Biologie,
F-33600 Pessac,
France

[4] School of Mathematics, Physics and Statistics,
Shanghai University of Engineering Science,
Shanghai 201620,
China

[5] Department of Biological Sciences,
Department of Chemistry,
Department of Bioengineering,
Lehigh University,
Pennsylvania 18015,
USA

[6] Institut de Pharmacologie et Biologie Structurale (IPBS),
Université de Toulouse, CNRS,
Université Toulouse III – Paul Sabatier,

31400, Toulouse,
France

[7] Laboratoire de Physique Théorique,
Université de Toulouse, CNRS,
UPS, Toulouse,
France

[8] Department of Chemistry,
University of Warwick,
Coventry,
CV4 7AL,
UK

+ equal contribution

*to whom correspondence should be addressed:
e-mail: wonpil@lehigh.edu
phone: +1 (0) 610-758-4524

e-mail: phillip.stansfeld@warwick.ac.uk
phone: +44 (0) 2476523864

e-mail: matthieu.chavent@ipbs.fr
phone: +33 (0) 5-61-17-59-00

Abstract

Mycobacterium tuberculosis (*Mtb*) is the causative agent of tuberculosis (TB), a disease that claims ~1.6 million lives annually. The current treatment regime is long and expensive, and missed doses contribute to drug resistance. Therefore, development of new anti-TB drugs remains one of the highest public health priorities. *Mtb* has evolved a complex cell envelope that represents a formidable barrier to antibiotics. The *Mtb* cell envelop consists of four distinct layers enriched for *Mtb* specific lipids and glycans. Although the outer membrane, comprised of mycolic acid esters, has been extensively studied, less is known about the plasma membrane, which also plays a critical role in impacting antibiotic efficacy. The *Mtb* plasma membrane has a unique lipid composition, with mannosylated phosphatidylinositol lipids (phosphatidyl-*myo*inositol mannosides, PIMs) comprising more than 50% of the lipids. However, the role of PIMs in the structure and function of the membrane remains elusive. Here, we used multiscale molecular dynamics (MD) simulations to understand the structure-function relationship of the PIM lipid family and decipher how they self-organize to shape the biophysical properties of mycobacterial plasma membranes. We assess both symmetric and asymmetric assemblies of the *Mtb* plasma membrane, and compare this with residue distributions of *Mtb* integral membrane protein structures. To further validate the model, we tested known anti-TB drugs and demonstrated that our models agree with experimental results. Thus, our work sheds new light on the organization of the mycobacterial plasma membrane. This paves the way for future studies on antibiotic development and understanding *Mtb* membrane protein function.

Significance statement

Understanding the biophysical properties of mycobacterial membranes is of crucial interest, especially in the context of drug discovery, but there is no realistic model of mycobacterial membranes. In this work, we have developed models of inner membrane of mycobacteria mainly constituted of mannosylated phosphatidylinositol lipids. Our results provide significant and unexpected insights into the molecular details of mycobacterial membranes. Especially, they highlight how recently determined proteins can accommodate into this specific membrane and how its lipid composition can affect antibiotics diffusion.

Introduction

Tuberculosis (TB) is caused by *Mycobacterium tuberculosis* (*Mtb*). In 2021 alone, there were an estimated 10.6 million new *Mtb* infections, leading to 1.6 million deaths (1). Thus, *Mtb* is one of the world's leading infectious killers, despite the availability of both a treatment regime and vaccine. The current course of antibiotics for drug susceptible TB cases can last as long as 6 months and consists of four drugs given in combination (2). This is not only expensive and demanding for the patient, but also encourages non-compliance that contributes towards the rise in multi-drug resistant and extremely drug-resistant TB (3). It is obvious that new treatments and a better vaccine are needed to meet the World Health Organization's 'End TB Strategy'. Their plan aims to reduce TB-related deaths by 90% by 2030, and thereby curtail the enormous public health cost caused by TB (4). The COVID-19 pandemic has undone some of the progress that had been made in the treatment of TB as fewer people were able to be diagnosed or access medication (5), which might result in a worldwide surge of untreatable cases. Thus, there is a pressing need for innovative research into the mechanisms of *Mtb* virulence and its ability to survive within the host for extended periods to help develop alternative intervention strategies.

One issue in anti-TB drug discovery is the complexity of the mycobacterial cell envelope (6, 7). This cell envelope consists of an array of lipids contributing to both hydrophobic and polar regions of various thicknesses and densities, making it extremely challenging to predict how molecules will cross this barrier and enter the cell. The *Mtb* cell envelope has four distinct layers: the outer layer (or the *mycomembrane*) comprised of mycolic acid esters and other complex lipids (such as phthiocerol dimycoserosates), an arabinogalactan-peptidoglycan layer, the periplasmic space and the inner membrane, or the plasma membrane (8). The mycobacterial plasma membrane plays a key role in controlling nutrient/antibiotic uptake and contains important membrane proteins that are targets for antitubercular drugs (9), such as SQ109 that inhibits the transporter MmpL3 (10). The membrane composition is also known to change during different growth stages of the bacteria (7) and may modulate drug and membrane protein diffusion. Additionally, recent studies showed that *Mtb* plasma membrane organization, such as the formation of functional membrane microdomains (11, 12), can affect the survival ability of mycobacteria. Therefore, understanding the molecular organization and dynamics of the *Mtb* plasma membrane is essential for developing effective drug candidates.

The mycobacterial plasma membrane is composed of a variety of lipids and glycolipids, the most abundant being (**Figure 1A**): cardiolipin (CL), phosphatidylethanolamine (PE), phosphatidyl-*myo*inositol (PI), trehalose monomycolate (TMM) and phosphatidyl-*myo*inositol mannosides (PIMs) (13), with the PIMs accounting for over half the dry weight of the plasma membrane lipids (13). PIM_2 lipids are comprised of a modified PI core decorated with two mannose residues and one acyl chain (**Figure 1B**). Furthermore, additional modifications of an acyl group and up to 4 mannose sugars can be added to the core headgroup, further diversifying the PIM structure (14, 15) (**Figure 1B** and **SI Figure 1**). It is still unclear if the plasma membrane is symmetric or asymmetric (16). In one widely cited and accepted study, it is proposed to be asymmetric (13), with Ac_2PIM_2 being the dominant species in the cytoplasmic leaflet accompanied by $AcPIM_2$, while the periplasmic leaflet is more varied, containing $AcPIM_2$, $AcPIM_6$, Ac_2PIM_6, CL, PI, PE and TMM (6, 13, 17, 18). PIM_6 lipids can be further modified to LM and LAM that make up the bulk of the periplasmic space (19). Additionally, lipids have been shown to modulate membrane protein function (20, 21). However, due to the complexity of the mycobacterial cell envelope, the dynamics and properties of the plasma membrane is extremely difficult to probe experimentally.

Over the last decade, molecular dynamics (MD) simulations have emerged as a powerful strategy for studying structural and functional aspects of biomembranes (22, 23). However, at the time of writing, there are no complete models of the mycobacterial plasma membrane that capture a possible asymmetry and the diverse range of lipids (24). This limits our ability to understand *Mtb* plasma membrane biology, model drug-lipid interactions - important for anti-TB drug discovery efforts - and simulate mycobacterial membrane proteins in a native environment. Therefore, it is essential to develop models of the major phospholipids of the mycobacterial plasma membrane for application in MD simulations.

Herein, multiscale simulations were used to analyze the structure-function relationship of the four main PIM lipids ($AcPIM_2$, Ac_2PIM_2, $AcPIM_6$ and Ac_2PIM_6) found in the mycobacterial membrane. An asymmetric bilayer containing these lipids was assembled and simulated, showing the stability of this composition. To highlight the robustness of our approach, additional simulations representing (in total) two different asymmetric growth stages as well as symmetric membrane configurations were performed. Systematic analysis of the distribution of *Mtb* protein residues in contact

with lipids reveals further indications that this membrane could possibly be asymmetric. We have also modelled how antibiotics, used to treat TB infections, diffuse through the membrane and interact with membrane proteins and demonstrated that our models agree with experimental results (25). Overall, we have developed robust possible representations of the mycobacterial plasma membrane that will enable studies of membrane dynamics, lipid interactions with integral membrane proteins, and diffusion of antibiotics across this barrier.

Methods

Building the coarse-grained lipid parameters

The CG models of the lipids were parametrized for the newly released MARTINI 3 force field (26) and generated using the protocol described for small molecules (27) on the MARTINI website (http://cgmartini.nl/index.php/martini-3-tutorials/parameterizing-a-new-small-molecule). The bead types and mapping to the PIM molecules were performed manually, comparing with the recently published CG model of PI (28). Atoms were grouped according to functional groups, in sets of 3-5 non-hydrogen atoms. The CG mapping of Ac_xPIM_x is shown in **Figures 1B,C**. The parameter files that describe the bonds, constraints, and angles were assembled based on the previously described data (26, 28, 29) as an initial estimate.

Simulations of each lipid were set up using a modified version of *insane.py* python script (30), embedding one copy of a PIM lipid in a 10 x 10 nm^2 phosphatidylcholine (PC) bilayer. The system was solvated with MARTINI water (26) and neutralized with 150 mM NaCl, followed by minimization using the steepest descents algorithm. The system was then simulated for 3 μs using a timestep of 20 fs at 310 K. The lipids, solvent and ions were temperature coupled separately. The velocity rescale (31) and Parrinello-Rahman (32) coupling methods were used with the time constants τ_T = 1.0 ps and τ_p = 12.0 ps for temperature and pressure, respectively. Simulations were run using GROMACS version 2021.3 (33). The reaction-field algorithm (34) was used for electrostatics interactions with a cut-off of 1.1 nm. A single cut-off of 1.1 nm was used for the van der Waals interaction. Five repeats were performed for each lipid (**SI Figure 2**).

Generating atomistic data

Parameters for the atomistic (AT) Ac_xPIM_x lipids were generated using the CHARMM force field (35). The CHARMM-GUI (36) server was used to set up the lipid systems for GROMACS with the CHARMM36m force field (37, 38). One PIM lipid was embedded in an 8 x 8 nm^2 PC bilayer. The system was solvated with 150 mM NaCl and minimized and equilibrated as per the CHARMM-GUI Membrane Builder workflow (39). The system was further minimized using the steepest descents. Simulations were run for 2 μs using a timestep of 2 fs at 310 K. The lipids, solvent and ions were temperature coupled separately. The velocity rescale (31) and C-rescale coupling methods were used with the time constants τ_T = 0.1 ps and τ_p = 1.0 ps for temperature and pressure, respectively. Simulations were run using GROMACS version 2021.3 (33). The particle mesh Ewald (PME) (40) method was used for electrostatic interactions with a cut-off of 1.2 nm. A single cut-off of 1.2 nm was used for the van der Waals interaction. Three repeats were performed for each lipid (**SI Figure 2**).

Refining coarse-grained parameters

The AT and CG representations of the four main PIM lipids are shown in **Figure 1C**. The distributions of the distances and angles were measured using the *gmx* tools (*distance*, *gangle* and *analyze*). For the AT simulations, the atoms were grouped according to their mapping and its center of geometry was used for calculations. The values for each bond/constraint and angle were iteratively refined based on the comparison of probability distribution, and the results are summarized in **SI Figures 3-8**. When there was agreement between the AT and CG data, the solvent accessible surface area was measured using the *gmx sasa* tool to verify that the models behaved the same (**SI Figure 8C**). Diffusion, shape of the lipids, clustering of ions, aggregation and interaction with other lipids were also measured on a single lipid level (**SI Methods** and **SI Figures 9-19**). As typical for MARTINI (41), dihedral terms are not defined in the parameters.

Measuring area per lipid

Before setting up the complete bilayer system, the area per lipid was measured. The simulations were assembled as described above for CG, using a homogenous Ac_xPIM_x membrane (**SI Figure 2**). The area of *XY*-dimension was measured using *gmx energy* and then dividing the area by the number of lipids in one leaflet over the

course of the trajectory, and the final values were extracted using *gmx analyze*, as per the protocol described on the MARTINI website (http://cgmartini.nl/index.php/tutorials-general-introduction-gmx5/bilayers-gmx5#Area-per-lipid).

Bilayer composition and set-up

The ratio of lipids in each bilayer was obtained by using their molecular weight and the previously reported dry masses (13) of the individual lipids, and the exact calculations can be seen in **SI Figure 20**. Since specific apolar lipids were not named, they were not included in this study. TMM was not included as there is no available refined AT model, the behavior of the mycolic acid is predicted to be complicated (42), and there is a relatively small proportion of TMM predicted to be present in the plasma membrane. The final composition of the plasma membrane is shown in **Figure 1A**.

The PI and PE lipids in mycobacteria are slightly different in structure to the corresponding *E. coli* lipids described in the MARTINI force field (26, 28): a methyl group replaces the alkene found in one of the acyl chains (**SI Figure 1**). Before assembling the membrane, the parameters for these lipids were modified by adapting the refined Ac_2PIM_2 acyl tail parameters and changing the existing tail. The CL parameters were transferred over from the MARTINI 3 beta force field (21).

Simulations of the bilayer were set up using a modified version of *insane.py* python script (30) using the composition shown in **Figure 1A**, where the area per lipid for the periplasmic membrane was set to 0.92 nm^2 and the cytoplasmic leaflet set to 1.13 nm^2. The systems were then treated the same as described for the initial CG systems with added equilibration steps as per the Membrane Builder workflow (39) before the production simulation. There were two types of system assembled to represent the asymmetric membrane previously mentioned (13). The first one had an initial simulation box size of 20 x 20 x 15 nm^3 and one repeat was performed for 10 μs at 290 K, 300 K, 310 K, 320 K and 350 K (**Figure 2A**). The second one had an initial box size of 50 x 50 x 15 nm^3 and a single repeat was performed for 10 μs at 310 K (**Figure 2C** and **SI Figure 2**). The number of lipids in each system is summarized in **SI Figure 21**.

To test how the membrane properties change with differing compositions, the same assembly procedure was followed to set up a symmetric membrane and an 'PIM-enriched' membrane (**SI Figure 22**), with one repeat for each in a simulation box of 20 x 20 x 15 nm^3, and another in a box of 50 x 50 x 15 nm^3, both at 310 K (**SI Figure**

2). Another membrane to capture an experimentally extracted membrane was simulated for 10 μs in a 20 x 20 x 20 nm^3 simulation box at 310 K. The number of lipids in each system is summarized in **SI Figure 21** and their compositions in **SI Figure 22**

Behavior of the membrane

To calculate the bending rigidities, the strategy proposed by Fowler *et al*. (43) to extract the bending modulus from CG simulations was followed. The membrane midplane position in Monge representation was determined by extracting the coordinates of all CG beads at the extremities of lipid fatty acid chains. Using a built-in function of the Mathematica software package, the positions were interpolated to get a smooth function before Fourier-transforming with a fast Fourier transform algorithm. From the so-obtained Fourier modes, the spectral density (or power spectrum) was estimated for a tensionless membrane:

$$S(q) = L^2 k_B T \left(1/(\kappa q^4) + 1/\left(\sigma_p r q^2\right)\right)$$

where L^2 is the projected area in the (x, y) plane, $k_B T$ is the thermal energy and $\sigma_p r \sim 0.1$ J/m^2 is the tension associated with lipid protrusions at the nanometer scale. $S(q)q^4$ was plotted as a function of q and fit it with a second order polynomial $P(q) = a + bq^2$, from which estimates of κ (and $\sigma_p r$ if needed) were obtained (**SI Figure 23**). The error bars are standard deviations provided by the fitting function in Mathematica.

The density of each constituent was measured using *gmx density* (**Figure 2B**). Diffusion, bilayer thickness and number of neighbors was measured using LiPyphilic (44) (**Figures 2D,E**, **SI Methods** and **SI Figures 24-27**). The xy-positions of single lipids were tracked with PLUMED (45) (**Figure 2E**). Area per lipid for the membrane was calculated using FATSLiM (46) (**Figure 2F**). Plots were created using Matplotlib (47).

Analysis of the residue distribution in membrane proteins

All predicted protein structures from *Mtb* (taxonomy id:83332) and *E. coli* (taxonomy id:83333) labelled as transmembrane on UniProt (48) were downloaded from the AlphaFold database (49), totaling 729 for *Mtb* and 1,229 for *E.coli*. Alphafold was used to obtain a workable dataset of structures, expanding upon the number of experimentally determined *Mtb* and *E. coli* membrane protein structures available from the PDB. Each of 1,958 membrane protein structures was orientated in a membrane

using memembed (50) with the *-n in* flag, then converted to CG using martinize2 (51) and inserted into either the asymmetrical mycobacterial (see **Figure 1A**) or *E. coli* membrane (75% PE, 15% PG, 10% CL) using a modified version of the *insane.py* python script (30). Each system was simulated for 10 ns. The residues within 8 Å of the lipids were selected and the density over the z-coordinate plotted (**Figure 3, SI Figure 28**).

Antibiotic simulations

Bedaquiline (BDQ) and isoniazid (ISZ) were mapped to CG using PyCGTOOL (52) following 200 ns AT simulations with parameters from CHARMM-GUI (53) (**Figure 4A**). The pK_a of the amine in BDQ is 8.91 (54), suggesting it will be protonated at physiological pH. This was considered when assigning the MARTINI 3 bead type (**Figure 4A**). To validate the use of the protonated state, the same simulations with a neutral BDQ molecule were performed and analyzed (**SI Figures 29A-C**). This was done by replacing the Q1 particle with a SC3 bead type (**Figure 4A**). In addition, the LogP for these antibiotics were calculated by perturbing the antibiotic in a box containing 878 MARTINI waters or 363 octanol and 32 waters. The Lennard-Jones parameters for each molecule were decoupled over 11 evenly spaced λ windows, for 50 ns per window. Simulations were run with 20 fs time steps in the NPT ensemble with the V-rescale thermostat at 323 K and an isotropic Parrinello-Rahman pressure coupling. Free energies were then computed using *gmx bar* and converted to water/octanol partitioning constants. The values were then compared to data from the ALOGPS online server (55). Alongside this, *gmx sasa* was used to calculate the solvent accessible surface area for the antibiotics in both CG and AT. The calculations were performed with 4800 dots per sphere and a probe size of 0.4 nm. Modified van der Waals radii for CG beads of 0.264, 0.230, and 0.191 nm for R, S and T beads were used respectively. For the Connolly surface generation, the calculations used 240 dots and a probe of 0.4 nm (**SI Figure 30**).

BDQ was first simulated with the mycobacterial membrane alone to confirm association with the membrane (**SI Figures 2,31**). The *Mtb* a- and c-subunits of F-ATPase, BDQ's target in the mycobacterial membrane, was modelled using SwissModel (56) based on a structure from *Mycobacterium smegmatis (25)* (PDB: 7JGC, **Figure 4C** and **SI Figures 32A,B**). The sequence identity between *Mtb* and *M. smegmatis* for the F-ATPase was calculated using Clustal Omega (57) at 80% and

72% for c- and a-subunits, respectively. The system with the protein in the asymmetric mycobacterial membrane (see **Figure 1A**) was assembled using martinize2 (51), memembed (50) and the modified *insane.py* python script (30), with eight molecules of BDQ placed either in the periplasmic or cytoplasmic leaflet with five repeats in each membrane (**SI Figure 2**). Simulations were run for 10 μs using the same setting as described above. The xyz-positions of BDQ, the lipids and the backbone beads were tracked over the course of the simulations with PLUMED (45) and plotted with Matplotlib (47), and the results are shown in **Figure 4D** and **SI Figures 32C,D, 33**. The density of each constituent was measured using *gmx density* and plotted using Matplotlib (47) and the results are shown in **Figure 4E** (with representative positions shown in **Figure 4F**). The interaction of BDQ with the protein was calculated using PyLipID (58) (**Figure 4G** and **SI Figures 34,35**). The same simulation set up was performed with a model *E. coli* membrane (75% PE, 15% PG, 10% CL) and with the symmetric mycobacterial membrane (**SI Figure 22A**). The z-position of BDQ is shown in **SI Figure 32** and **SI Figures 36,37**.

PMF calculations

The potential of mean force (PMF) calculations for the F-ATPase-BDQ interaction were performed (59). First, a representative pose of BDQ bound to the protein was produced using PyLipID from equilibrium simulations and built into a 12 x 20 x 11 nm^3 asymmetric mycobacterial membrane (see **Figure 1A**) membrane and minimized and equilibrated, as described above. Light (50 kJ/mol/nm^2) *xy* positional restraints were added to Ala 66 on three c-subunits to prevent the protein from rotating in the membrane. Following 50 ns of equilibration, the BDQ was steered away from the protein along the *y* axis at a rate of 1 nm/ns with a 1,000 kJ/mol/nm^2 restraint potential. Frames were extracted at 0.1 nm spacing along this coordinate to seed a total of 58 x 1.5 μs production simulations with a static 1,000 kJ/mol/nm^2 umbrella potential imposed to keep the system in the same position along the reaction coordinate. The PMF mdp input files can be downloaded at https://github.com/chelsea-brown/PIM-lipids/tree/main/PMF-files. The PMF profiles were then constructed using the weighted histogram analysis method in GROMACS (*gmx wham* (60, 61)*,* and employing 200 rounds of Bayesian bootstrapping to report statistical accuracy (**Figure 4H**).

For the membrane crossing PMFs, BDQ or ISZ was placed free in the solvent phase, 7 nm away from the membrane periphery in either an asymmetric

mycobacterial membrane (see **Figure 1A**) or *E. coli* membrane. The drug was then steered towards and through the membrane and into the solvent phase on the other side. Windows were extracted, simulated (1 μs for ISZ per window and 2 μs per window for BDQ) and analyzed as described above (**Figure 4B** and **SI Figure 29D** for BDQ neutral). The -cycl option was imposed when running *gmx wham.*

Results

PIM properties

As an initial step towards developing an *in-silico* model of the mycobacterial plasma membrane, we first examined lipid properties in our CG and AT models. As shown in **SI Figures 3-8**, the probability distributions of bonds and angles from the CG and AT simulations align well, which illustrates that the behavior of the acyl chains is similar to other phospholipids (30). The Ac_xPIM_x aggregation in the AT and CG simulations is comparable and shows no permanent clustering. When lipids did come into contact, all areas of the molecule appear to play an equal role in the interactions (**SI Figures 15,17**). The interactions were not dominated by the sugars, as was seen with the previous iteration of the MARTINI 2 force field (62), and the phospholipids present in the mycobacterial membrane did not have strong interactions with the PIM lipids (**SI Figure 18,19**). The PIM lipids show a higher affinity for ions than PC in CG simulations, but the effect is less apparent in AT simulations (**SI Figure 14**). While the ion concentrations were the same, the number of ions in the simulation box were different (an order of magnitude higher for CG), which could explain these results. Overall, CG simulations of these lipids behave similarly to AT models (interactions with ions as a minor exception), therefore opening the door to significantly longer simulations by decreasing the degrees of freedom in the system.

The area per lipid in CG for each species in a PC bilayer was found to be 0.93 nm^2 ($AcPIM_2$), 1.15 nm^2 (Ac_2PIM_2), 1.01 nm^2 ($AcPIM_6$), 1.14 nm^2 (Ac_2PIM_6), 0.6 nm^2 (PI), 0.55 nm^2 (PE) and 1.25 nm^2 (CL). The diffusion coefficients for each PIM species in a PC bilayer at 310 K are as follows: 6.7 x 10^{-7} cm^2/s ($AcPIM_2$), 1.1 x 10^{-7} cm^2/s (Ac_2PIM_2), 7.6 x 10^{-7} cm^2/s ($AcPIM_6$), 6.5 x 10^{-7} cm^2/s (Ac_2PIM_6) (**SI Figure 9**). The difference between $AcPIM_x$ and Ac_2PIM_x shows the effect of the extra acyl tail in terms of how freely these lipids diffuse through the membrane.

The lipid shapes are approximately the same from AT to CG (**SI Figures 10-13**), which agrees with the comparison of the surface areas (**SI Figure 8C**) and the sugar-phosphate z-distances in Ac_xPIM_6 (**SI Figures 5C,7C**). The additional mannose moieties project upwards away from the membrane in both sets of simulations. Interestingly, the lipid tail region is measured to occupy approximately the same amount of space with three or four acyl chains. This is likely due to the placement of the fourth tail, projecting downwards from the inositol sugar (as highlighted in red in **Figure 1B**) and hence inhabiting space close to the other acyl chains.

Taken together, the lipid properties in our CG model broadly replicate those seen with AT resolution. This provided the confidence to assemble these lipids into a complex bilayer.

Mycobacterial membrane biophysical properties

Traditional MD simulations of bacterial membranes use symmetric bilayer representation. However, a study has shown that the mycobacterial plasma membrane could be an asymmetric bilayer, and we used the published composition of the mycobacterial plasma membrane (13) (**Figure 1A**) (excluding apolar lipids and TMM) to assemble an asymmetric bilayer (**Figures 2A,C**). This bilayer was found to be stable during 10 μs simulation (**SI Movie 1**), and in good agreement with the literature (8, 13). The thickness of the plasma membrane in our simulations was at 5.3 ± 0.1 nm (**Figure 2B**), which is slightly narrower than values obtained from imaging studies (6.3 nm for *Mycobacterium bovis* and 7 nm for *Mycobacterium smegmatis*) (63-65). However, we did observe thicknesses of up to 7 nm in the density plot (**Figure 2B**). *In vitro* culture conditions or growth stages of the bacteria (65) impact the thickness on the membrane and could explain any minor differences with our model.

To test the phase behavior of this membrane, we performed simulations at various temperatures ranging from 290 K to 350 K. For the whole range of temperatures, lipids were in the liquid phase and allowed to diffuse freely (**Figure 2E** and **SI Figure 24**). The calculated diffusion coefficients for each species in the periplasmic leaflet at 310 K were as follows: 9.9×10^{-8} cm^2/s ($AcPIM_2$), 6.9×10^{-8} cm^2/s ($AcPIM_6$), 1×10^{-7} cm^2/s (Ac_2PIM_6), 1.3×10^{-7} cm^2/s (PI), 1.5×10^{-7} cm^2/s (PE) and 1.2×10^{-7} cm^2/s (CL). In the cytoplasmic leaflet, the values were 6.1×10^{-8} cm^2/s ($AcPIM_2$) and 8.1×10^{-8} cm^2/s (Ac_2PIM_2). Compared to isolated PIMs in a PC membrane, the diffusion in this plasma membrane was roughly one order of magnitude slower.

$AcPIM_2$, which is the only lipid in both leaflets, diffused ~40% slower in the cytoplasmic membrane compared with the periplasmic leaflet. Using a previously reported model of mammalian plasma membrane (22), the diffusion coefficients of PE and PI were calculated to be 3.3 x 10^{-7} cm^2/s and 2.8 x 10^{-7} cm^2/s, showing that the diffusion in the mammalian membrane is equivalent to that in the mycobacterial plasma membrane. The membrane stiffness of our mycobacterial membrane was significantly lower at κ =8.2 k_BT compared to 13.9 k_BT and 19.1 k_BT for the mammalian and PC membrane models, respectively (**SI Figure 23**), highlighting a unique dynamic behavior for the mycobacterial plasma membrane.

Lipid clustering was moderate and membrane composition remained heterogenous over the course of each 10 μs simulation (**Figure 2C**). This can also be seen in **Figure 2D** where the number of surrounding lipids of the same type for each species in the periplasmic membrane was roughly equivalent to that of any other lipid species. The distribution of the area per lipid in the membrane also suggests high heterogeneity (**Figure 2F**). The average area per lipid in the membrane over the course of the simulation was 0.89 nm^2 and 1.18 nm^2 for the periplasmic and cytoplasmic leaflets, respectively. Thus, the cytoplasmic leaflet appears to be a little denser than the periplasmic leaflet. This can be related to the packing of the four acyl chains of Ac_2PIM_2 lipids present in high concentration in this leaflet (66). A movie for the change in area per lipid for each leaflet over the course of the simulation can be found in **SI Movies 2,3**.

As was seen for the individual lipids in CG the overall bilayer attracted ions; both Cl^- and Na^+ concentration was much higher close to the bilayer, especially around the sugar head groups compared to bulk solution (**Figure 2B**). It has been shown that lipid-ion interactions can affect the biophysical properties of the membrane, such as fluidity and stiffness, as well as the structure, which could modify the interaction with proteins (67).

The mycobacterial plasma membrane has been reported to change at different growth stages (7, 68), but the study that originally proposed the composition was based solely on late-exponential-phase cells. To explore a wider range of possible membrane compositions, we designed an 'PIM-enriched' bilayer, where the amount of PIM lipids in the periplasmic leaflet was increased to reflect cells in rapid growth (7) (see compositions in **SI Figure 22**). In this case, the overall biophysical properties of that leaflet were very similar to those seen in **Figure 2**, but interestingly a change in

the diffusion and density of the cytoplasmic leaflet was observed (**SI Figures 26,27**). Increasing the proportion of lipids in the periplasmic leaflet that have 3 or 4 acyl chains could mean that the lipid tails make more inter-leaflet interactions and hence slow down diffusion and make the leaflet denser. This decrease in fluidity in the membrane could impact antibiotic diffusion through the membrane (13, 69) which would make the bacteria less susceptible to treatment at a time when it is most vulnerable.

We have also tested alternative plasma membrane compositions with a symmetrical configuration. First, we performed a model of a membrane recapitulating the composition being experimentally derived using a combination of mass spectrometry and NMR (see composition in **SI Figures 22,38**). This symmetrical configuration is stable, and the dynamics of PIM lipids in CG-MD simulations agreed with solid state NMR results (see **SI Figures 38,39**). This data shows that the acyl chains extremities are highly mobile, while the core of the acyl chains displayed a more rigid structure. Interestingly, the sugar moieties adopted an intermediate dynamic regime, as seen from experimental NMR results (**SI Figure 38E**) and MD simulations (**SI Figure 39B**). We then designed a model of symmetrical membrane system with a lipid composition that mimics *Mtb* membranes (see composition in **SI Figure 22A**). This membrane showed similar interactions of lipids compared to the asymmetric composition and also similar rates of diffusion (**SI Figures 25,27**). Clustering of ions around the sugar headgroups was still observed.

Taken together our observations suggest that PIM lipids play a critical role in the dynamic and structuration of mycobacterial plasma membrane. Both the asymmetric and symmetric configurations of the membrane were equally stable and our analyses show that both share similar dynamic properties. This work demonstrates the plausible arrangements of the plasma membrane and provides a mechanism to easily study new membrane compositions based on future experimental results.

Asymmetrical distribution of residues at the surface of Mtb membrane proteins

The lipids of the plasma membrane do not exist in isolation, but rather in cooperation with membrane proteins. These proteins could provide insights into how this membrane exists natively (70). To explore this, we used the accurate, fast and reliable workflows of AlphaFold (49) and memembed (50), to insert all transmembrane proteins from *Mtb* and *E. coli* into their native-like membranes (**Figure 3A,B**). We then assessed the distribution of residues in proximity to the lipid bilayer (**Figure 3C**).

For *E. coli,* the distribution is as expected and similar to results previously shown (21). The asymmetry of Arg and Lys reflect the 'positive inside rule' (71-73) present in bacteria which aids in the correct insertion of the transmembrane helices. The symmetric nature of the lipid bilayer is otherwise reflected in the distribution of the residues (**Figure 3C**, **SI Figure 28**). The *Mtb* distribution of Arg also shows a strong 'positive inside rule'. This is at a higher intensity than in *E. coli,* likely due to the low levels of Lys observed (**Figure 3C**). Furthermore, the decrease in the bulky Phe and Tyr residues (**Figure 3C**) in the cytoplasmic leaflet compared to the periplasmic leaflet agrees with the increased density seen in an asymmetric membrane (**Figure 2B** and **SI Figure 26B**).

These results add evidence to an asymmetric model previously proposed (13). In addition to validating the model proposed in this work, it could aid understanding of how mycobacterial membrane proteins differ from those found in other organisms and hence aid targeted therapies.

Asymmetric interaction of the membrane with antibiotics

We were interested in testing how the organization of this membrane affects the behavior of other molecules, such as antibiotics. We tested two widely used anti-TB antibiotics: Isoniazid (ISZ) and Bedaquiline (BDQ) (**Figure 4A**). To validate the behavior of these small molecules as well as the bond lengths/angles being account for through PyCGTOOL (52) (**SI Figure 30**), the LogP and solvent accessible surface area were calculated for each and compared to predicted values and atomistic values, respectively. The values for LogP for neutral BDQ (5.92 for CG, 6.37 predicted) and ISZ (-1.10 for CG, -0.71 predicted) agree very well, as do the solvent accessible surface area values (BDQ values 13.01 ± 0.49 nm^2 for CG and 13.69 ± 1.11 for AT; ISZ values 7.48 ± 0.14 nm^2 for CG and 7.35 ± 0.04 for AT).

ISZ is a first line anti-TB treatment that targets InhA, a cytosolic enzyme that is essential for mycolic acid synthesis (74). BDQ on the other hand is a last line antibiotic that targets the membrane protein complex of the ATP synthase (75, 76). The PMF results for ISZ and BDQ show that the mycobacterial membrane behaves as expected regarding the passage of a small molecule through a lipid rich membrane, showing favorable interactions with the largely hydrophobic BDQ and unfavourable interactions with hydrophilic ISZ (**Figure 4B**). The positive charge present on BDQ could account for the sharp free energy barrier at the membrane midplane. To assess the effect of

541 the charge on the passage of BDQ since the protonation state is unknown, we
542 modeled a neutral BDQ where the charged Q1 bead (see **Figure 4A**) was replaced
543 by SC3. The PMF results with the neutral BDQ show a reduction in the energy barrier
544 at this point (**SI Figure 29D**). We note that the passage of these drugs through an *E.*
545 *coli* inner membrane is symmetric from the mid-plane of the membrane as expected.
546 The interactions of BDQ with the periplasmic leaflet of the mycobacterial membrane
547 were ~6 kJ/mol stronger than for the simple membrane and the mycobacterial
548 cytoplasmic leaflet. This is possibly due to the presence of tetraacylated PIMs in the
549 mycobacterial periplasmic leaflet. Roughly the same difference between the
550 mycobacterial and simple membranes was observed for ISZ at the mid-membrane
551 region, showing less favorable passage through the membrane. These results suggest
552 that ISZ, a first-line TB drug, is unlikely to freely diffuse through the membrane, which
553 is in contrast with the previously proposed uptake mechanism based on passive
554 diffusion (77-79). Small differences were seen for ISZ interactions at the interfaces of
555 the mycobacterial and simple membrane periplasmic membrane. This could be due to
556 the presence of certain PIM lipids in this leaflet. In our simulations, when the BDQ
557 starting position was in the bulk solvent, the drug quickly associated with the
558 membrane, as shown in **SI Figure 31**, and displayed no strong preference for either
559 leaflet in these simulations.
560 BDQ has been shown to target the mycobacterial ATP synthase (Rv1304-
561 Rv1311), a membrane protein complex. A cryo-EM structure from *M. smegmatis*
562 (PDB: 7JGC) shows multiple binding sites for BDQ at the interface of the c-subunits
563 and the interface between the a- and c- subunits (25), where a highly negatively
564 charged area is located (**SI Figure 32A,B**). Using the available cryo-EM data, we
565 performed 10 simulations of 10 μs each to examine how *Mtb* ATP synthase complex
566 behaves in our asymmetric mycobacterial plasma membrane model. ATP synthase
567 was stable in the membrane and that there were no significant perturbations of the
568 bilayer by the protein. The lipids of the mycobacterial membrane did not show any
569 strong interactions with the protein (**Figure 4D** and **SI Figure 33**), apart from CL that
570 localizes in the a-subunit and around the c-ring (**Figure 4D**) in positions similar to
571 those observed in a previous study (80). The exact values for CL occupancy of each
572 residue are shown in **SI Figure 35A**. Minimal interactions between BDQ and the
573 ATPase occurred when the drug started in the periplasmic leaflet; however, when BDQ
574 was introduced in the cytoplasmic leaflet, significant occupation of the binding sites on

ATPase were observed (**Figures 4D-G** and **SI Figures 32C,D**). The interactions were reduced with the neutral BDQ model (**SI Figures 29A-C**). Of note, no such leaflet differences were observed when we tested the *E. coli* symmetric membrane model (**SI Figures 36C,D**; **SI Figure 37**), but with a symmetric mycobacterial membrane (**SI Figure 32**). This suggests that the lipid composition plays a crucial role in the regulation of antibiotic interactions.

Furthermore, the interactions of the charged BDQ we observed matched well with what was previously seen in the cryo-EM structure (25), with an occupancy of ~30% of the simulation time on some subunits (**Figure 4G**). The occupancy value averaged over all subunits is shown in **SI Figure 35B**. The simulations were able to identify all three types of sites reported previously (25). Most interactions were seen through the leading site (46% of the time, K_{off} = 5.2 μs^{-1}) followed by the lagging site (22% of the time, K_{off} = 7.6 μs^{-1}) and finally further interactions around the rotor (36% of the time, K_{off} = 1.2 μs^{-1}, **SI Figure 34**). For the leading site, the PMF calculations confirm this as a binding site, giving a moderate energy well of approximately 7 kJ/mol (**Figure 4H**) and making it equivalent to a typical cholesterol-protein binding interaction (81). Tracking the z-position of the central bead from the antibiotic over the course of the unbiased simulations with the protein shows that the binding sites are occupied to some extent by each of the drug molecules and some are flipped to the outer leaflet from the plasma leaflet, as shown in **SI Figure 32C**.

These studies illustrate that our asymmetrical mycobacterial plasma membrane model can be combined with studies of antibiotics, as well as with studies of membrane proteins and their interactions with lipids and/or antibiotics. Taken together, our simulations suggest that BDQ must enter the target protein from the cytoplasmic side, which agrees with resistance mechanisms against BDQ that involve upregulation of MmpL5, a drug efflux pump (82, 83). Importantly, an *E. coli* membrane could not capture this feature, highlighting that the mycobacterial membrane model is a more accurate and functionally relevant representation of the *Mtb* plasma membrane.

Discussion

Here, we provide models for lipids constituting the mycobacterial plasma membrane focused on the PIM lipids, as they represent more than 50% of the total lipid content in *Mtb*. Thus, understanding how these lipids behave on an individual level and as a

609 constituent of a membrane could provide key insight into the intrinsic resistance of *Mtb*
610 to antibiotics.

611 In this CG model, clustering of ions around these lipids was observed at both
612 the single lipid and bilayer level, probing how this affects the biophysical properties of
613 the bilayer and whether this could be exploited for treatment of TB is an interesting
614 area for future research. The lipids did not cluster together excessively over the
615 timescales studied and all diffused well through the membrane. This confirmed that
616 the mycobacterial cell envelope is dynamic, which could potentially be an important
617 insight into how this cell wall functions. A low membrane bending rigidity compared to
618 a PC and eukaryotic plasma membrane is interesting and could suggest the
619 importance of other cell envelope components in maintaining the shape of the cell.

620 The simulations confirmed that our asymmetric plasma membrane model is
621 stable with a composition of over 50% PIM lipids. However, considering that this
622 arrangement has not been experimentally validated, a symmetric and 'enriched PIM'
623 asymmetric membrane was also shown to share similar biophysical properties. The
624 high proportion of PIM lipids resulted in some unique properties, most notably lower
625 membrane stiffness, which may have important implications for membrane
626 microdomain formation, drug penetration, and integral membrane protein behavior. In
627 this context, the integral membrane proteins from *Mtb* are of interest for the
628 development of new antibiotics for TB (9), and we show evidence that our membrane
629 model can be used to simulate proteins in a native lipid environment to determine any
630 key lipid interactions, as illustrated by our study of antibiotic BDQ and its target,
631 ATPase. In addition, an overall comparison of plasma membrane protein residues
632 found in contact with the lipid bilayer revealed differences between *Mtb* and *E. coli*,
633 supporting the asymmetric nature of the mycobacterial plasma membrane model. This
634 potentially hints at topological differences between proteins in mycobacteria and those
635 within other bacteria. If this is the case, currently unknown proteins which maintain the
636 asymmetry might be present (such as those identified in animal cells (84)), and would
637 constitute interesting drug targets to explore.

638 Potential limitations of our model stem from the reduced type of lipids we
639 included in this initial development. Thus, future studies will focus on expanding the
640 model to include apolar lipids (such as triglycerides (17)), TMM and LM/LAM.
641 Moreover, future simulations with proteins and probing protein/lipid interactions with
642 atomistic resolution could help further elucidate the role of these complex lipids.

In conclusion, our study is a starting point for building an entire mycobacterial cell envelope, as done for gram-negative bacteria (85). Other mycobacterial lipids have already been parameterized (86), and combining them with the model described here has the potential to significantly advance the field that has been lacking experimental strategies for plasma membrane investigations. Additionally, the mycobacterial cell envelope is known to change at different growth stages during its lifecycle (7, 68, 87, 88) and in response to different environments (69). With our model and set-up methods, as shown with the multiple compositions simulated, it will be possible to understand drug permeability or protein behavior at different stages of infection. Taken together, integrating our mycobacterial plasma membrane model into broader studies of this pathogen, its pathogen/host interactions, as well as into anti-TB drug discovery and development has a potential to reveal new functional insights and yield improved therapies.

Data availability: https://github.com/pstansfeld/PIM-lipids
Atomistic systems and CG-membrane set-up can be performed using respectively CHARMM-GUI bilayer builder (https://charmm-gui.org/input/membrane.bilayer) and CHARMM-GUI MARTINI bilayer Maker (https://charmm-gui.org/?doc=input/martini.bilayer)

Author contributions

C.M.B., R.A.C., W.I., P.J.S. and M.C. designed research; C.M.B., R.A.C., Y.G., Y.K.C. and E.L. performed computational research; C.M.B., R.A.C. and N.D. analyzed computational data; A.G., M.G., J.N. and A.L. performed experimental research and analysis; C.M.B., R.A.C., A.L., P.J.S. and M.C. wrote the paper; J.N., A.L., E.F., W.I., P.J.S. and M.C. obtained funding.

Acknowledgements

C. M. B. is supported by an MRC studentship (MR/N014294/1). R. A. C. is funded by Wellcome (208361/Z/17/Z). Research in P. J. S.'s lab is funded by Wellcome (208361/Z/17/Z), the MRC (MR/S009213/1) and BBSRC (BB/P01948X/1, BB/R002517/1 and BB/S003339/1). M. C. is supported by the CNRS-MITI grant "Modélisation du vivant" 2020. W. I. is funded by NSF (MCB-2111728). E.F is a Sir Henry Dale Fellow jointly funded by the Wellcome Trust and Royal Society (104193/Z/14/Z and 104193/Z/14/B). M. G. would like to acknowledge the

European Union's Horizon 2020 research and innovation program under grant agreement H2020-PHC-08-2014-643381, TBVAC2020. This work was granted access to the HPC resources of CALMIP supercomputing center (under the allocation 2021-17036) and TGCC Joliot-Curie supercomputer (under the GENCI allocation A0110712941). This project made use of time on ARCHER2 and JADE2 granted via the UK High-End Computing Consortium for Biomolecular Simulation, HECBioSim (http://hecbiosim.ac.uk), supported by EPSRC (grant no. EP/R029407/1). This project also used Athena and Sulis at HPC Midlands+, which were funded by the EPSRC on grants EP/P020232/1 and EP/T022108/1. This work has benefited from the facilities and expertise of the Biophysical and Structural Chemistry platform (BPCS) at IECB, CNRS UAR3033, INSERM US001, and Bordeaux University. We thank the University of Warwick Scientific Computing Research Technology Platform for computational access. We acknowledge Life Science Editors for proofreading the manuscript. We thank C. Cooper for fruitful discussions and M. Costic for comments on the manuscript.

Abbreviations

AT:	Atomistic
ATP:	Adenosine triphosphate
BDQ:	Bedaquiline
CG:	Coarse grained
CL:	Cardiolipin
ISZ:	Isoniazid
LAM:	Lipoarabinomannan
LM:	Lipomannan
MD:	Molecular dynamics
Mtb:	*Mycobacterium tuberculosis*
NMR:	Nuclear magnetic resonance
PC:	Phosphatidylcholine
PE:	Phosphatidylethanolamine
PG:	Phosphatidylglycerol
PI:	Phosphatidylinositol
PIMs:	Phosphatidyl-*myo*-inositol mannosides
PIPs:	Phosphatidylinositol phosphates
PME:	Particle mesh Ewald
PMF:	Potential of mean force
TB:	Tuberculosis
TMM:	Trehalose monomycolate
VdW:	van der Waal

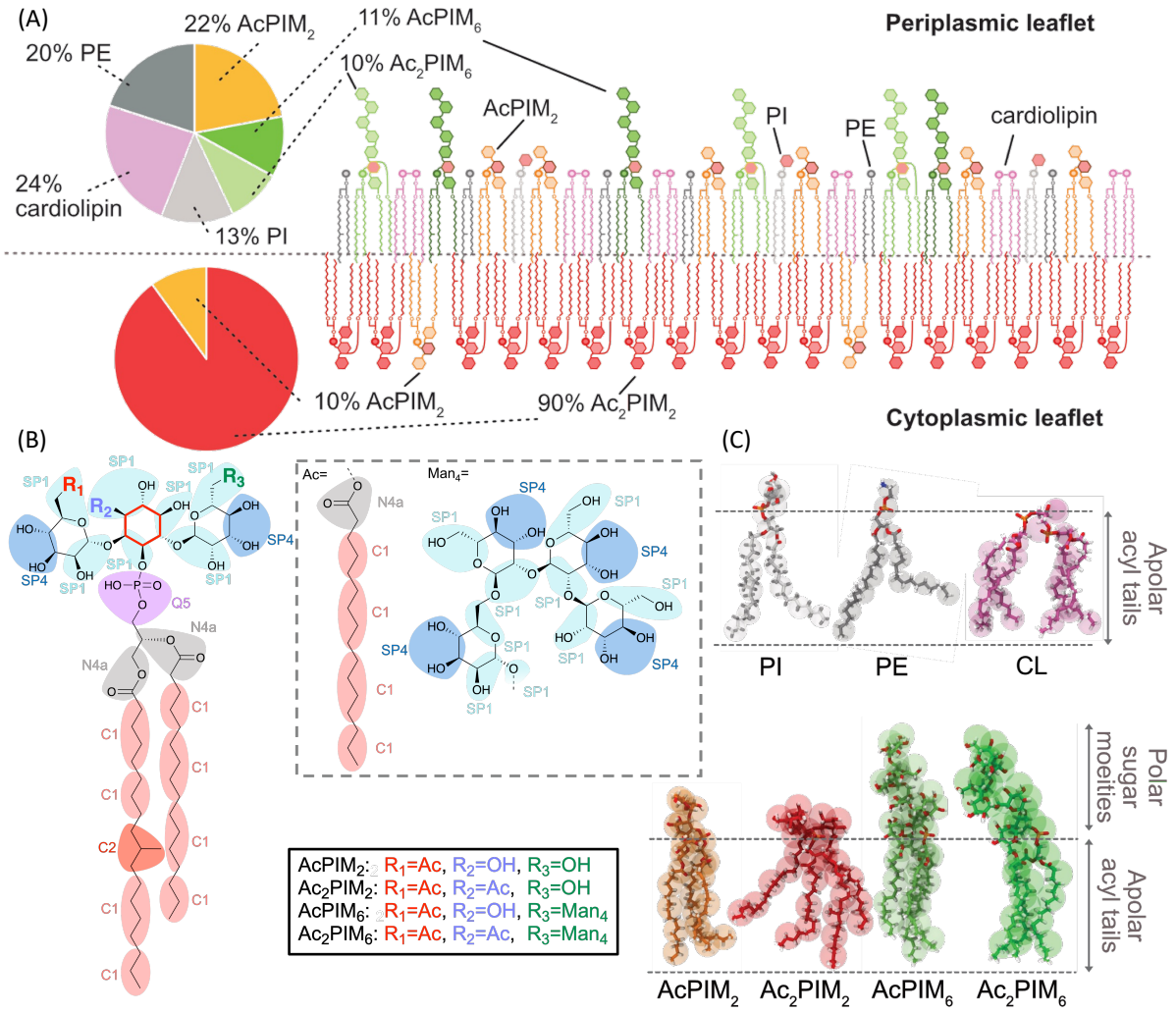

Figure 1: The structure of the mycobacterial lipids. (**A**) Schematic of an asymmetrical model of the mycobacterial plasma membrane and composition as previously defined (13). (**B**) Schematic of the core of the PIM lipids found in mycobacteria with the groupings for coarse-grained (CG) beads. The inositol core is highlighted in red. The bead types for MARTINI 3 are shown. (**C**) Overlay of the AT (sticks) and CG (spheres) models for each lipid, with chemical characteristics shown to the right.

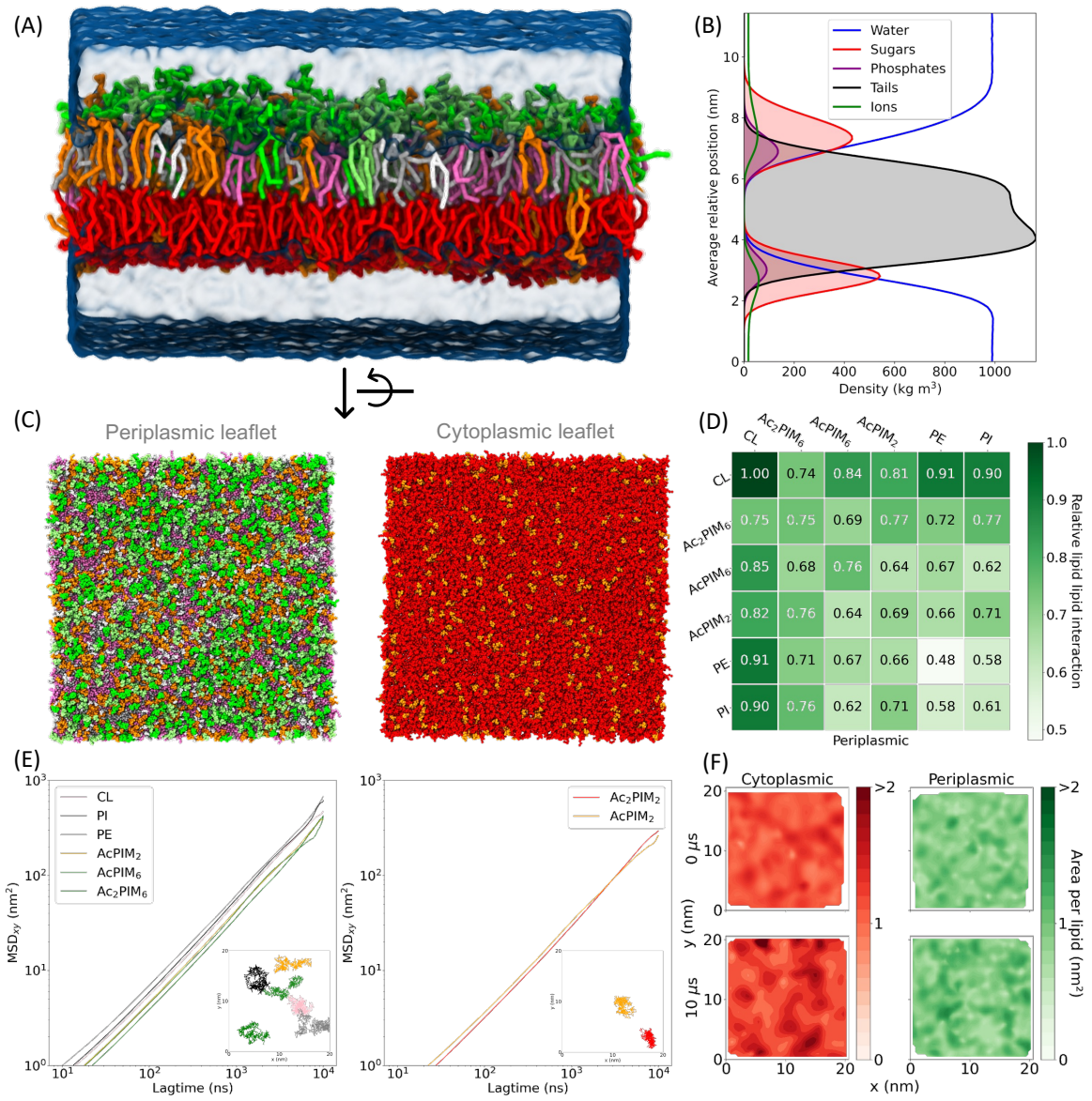

723

724 **Figure 2:** A mycobacterial membrane model. (**A**) Side view of the membrane with each lipid
725 type depicted in a different color as shown in **Figure 1A**. (**B**) A density plot showing the density
726 of water, sugar groups, phosphate groups, tail groups and ions over the simulation box. (**C**)
727 Snapshots of the periplasmic and cytoplasmic leaflets whose compositions are: $AcPIM_2$ 22%,
728 $AcPIM_6$ 11%, Ac_2PIM_6 10%, CL 24%, PE 20% and PI 13% (periplasmic leaflet) and $AcPIM_2$
729 10% and Ac_2PIM_2 90% (cytoplasmic leaflet). The system size is 50 x 50 x 15 nm. (**D**) Relative
730 number of neighbors of each lipid type for the periplasmic membrane. (**E**) Mean squared
731 displacement (MSD_{xy}) (nm^2) as a function of lagtime (ns) for each lipid type in the periplasmic
732 and cytoplasmic leaflets. The inserts show the position of the phosphate group of each lipid
733 type over the last 500 ns of the simulation. (**F**) Contour plots of the area per lipid (nm^2) in each
734 leaflet at the starting frame (upper) and final frame (lower) of the simulation. A darker color
735 indicates a larger area per lipid.

736

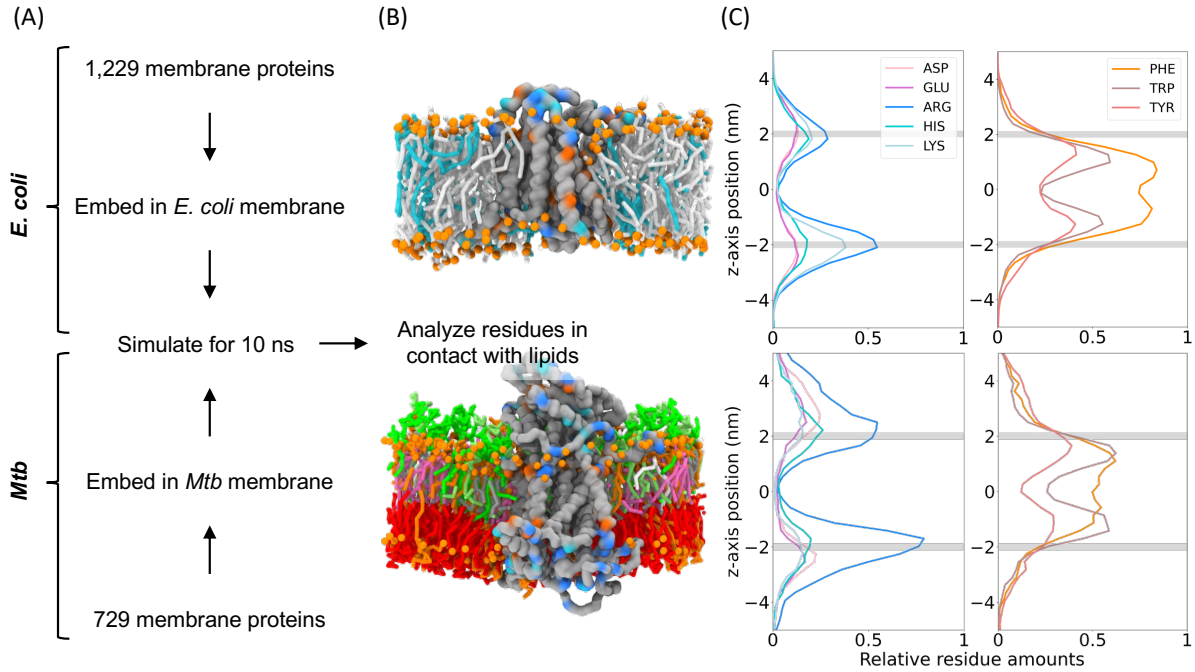

Figure 3: The asymmetry of the mycobacterial membrane. (**A**) A simplified workflow for the lipid contacts analysis from all membrane proteins. (**B**) An example of a protein (*E. coli* protein MraY UniProt id: P0A6W3 and *Mtb* transporter MmpL3 UniProt id: P9WJV5) embedded in either an *E. coli* or mycobacterial membrane. The orange spheres represent phosphates. For *E. coli* membrane the cyan sticks show PG and the grey sticks PE. For mycobacterial membrane, the lipid sticks are shown in the colors illustrated in **Figure 1A**. Selected residues are colored according to the key in (C). (**C**) Graphs for *E. coli* and *Mtb* (top and bottom respectively) showing the relative abundance of selected residues within 8 Å of lipids. The gray lines show the position of the phosphates. The cytoplasmic region is shown by negative z values, the periplasmic region by positive values.

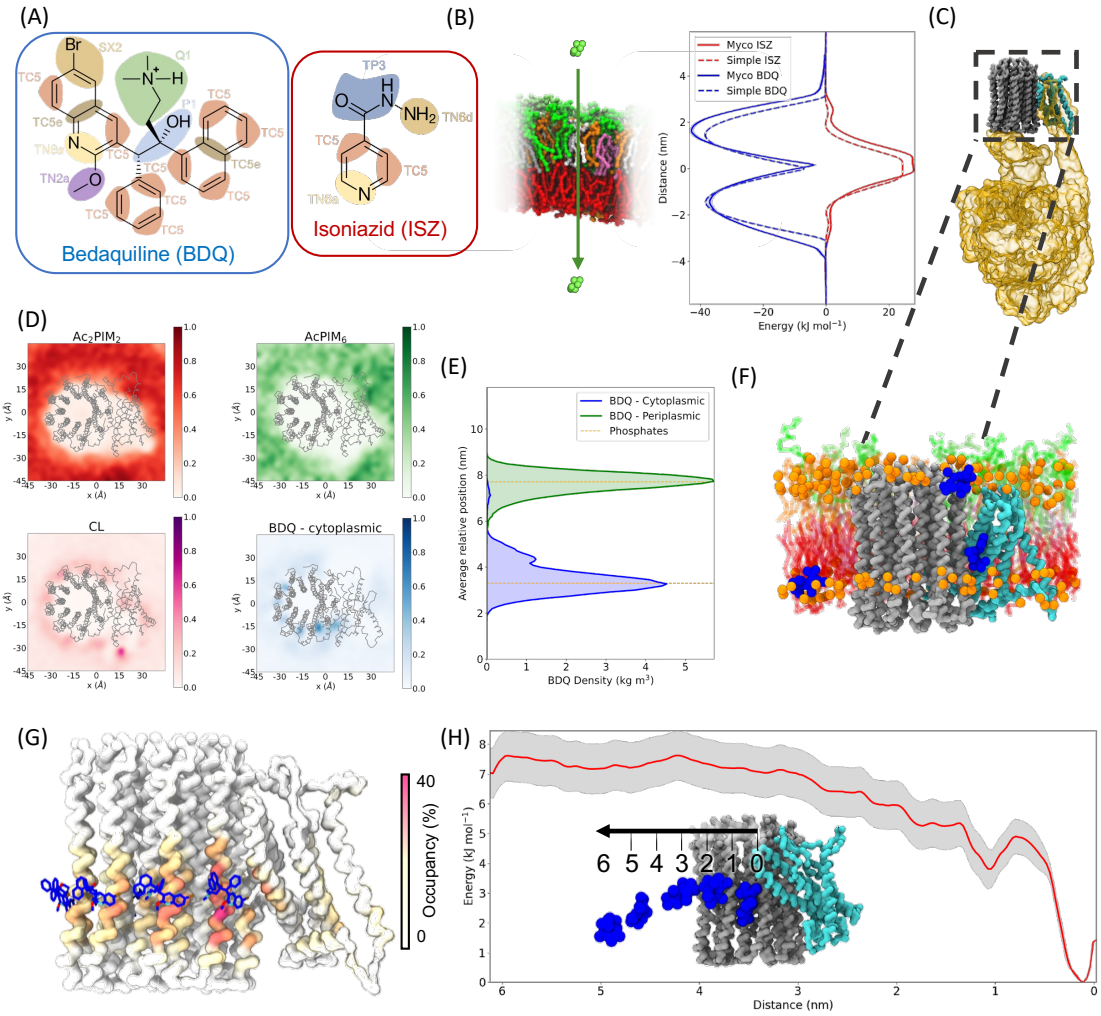

Figure 4: The behavior of the antibiotics with mycobacterial membrane and proteins. (**A**) Chemical structures of BDQ and ISZ with the CG groupings overlaid and bead types shown. (**B**) PMFs of the two antibiotics being pulled through either a mycobacterial or simple membrane in the z-direction. BDQ is shown in blue and ISZ in red, with the mycobacterial membrane results having a solid line and simple membrane having a dashed line. The error is shown in grey. A schematic of the PMF is shown to the left. (**C**) Structure of *Mycobacterium smegmatis* ATP synthase (PDB: 7JG5) with the c-subunits shown in grey, the a-subunit shown in cyan, and the other components shown as a gold surface. (**D**) Density in the x and y dimensions of selected lipids and BDQ when starting in the cytoplasmic leaflet relative to the protein shown in grey. (**E**) Density of the phosphates (orange) and BDQ over the course of the simulations where the antibiotic started in either the periplasmic leaflet (green) or the cytoplasmic leaflet (blue). (**F**) Snapshot of a single simulation containing a *Mtb* ATPase model and 8 x BDQ models showing the main positions BDQ occupied. Phosphates are shown in orange, BDQ shown in blue, c-subunits are shown in grey, and the a-subunit is shown in cyan. The lipid sticks are shown in the colors illustrated in **Figure 1A**. (**G**) Comparison of the highest occupancy sites identified with PyLipID (surface) and BDQ from the Cryo-EM structure (PDB: 7JGC) (sticks). (**H**) PMF of BDQ moving through a mycobacterial plasma membrane with the error shown in grey. A schematic of the PMF is shown as an insert.

References

1. WHO (2022) Global tuberculosis report 2022. (World Health Organization, Geneva).
2. C. R. Horsburgh, C. E. Barry, C. Lange, Treatment of Tuberculosis. *New England Journal of Medicine* **373**, 2149-2160 (2015).
3. WHO (2021) Global Tuberculosis Report 2021. (World Health Organization, Geneva).
4. WHO (2022) The End TB Strategy.
5. WHO (2021) 1.4 million with tuberculosis, lost out on treatment during first year of COVID-19.
6. L. Chiaradia *et al.*, Dissecting the mycobacterial cell envelope and defining the composition of the native mycomembrane. *Scientific Reports* **7**, 12807 (2017).
7. C. L. Dulberger, E. J. Rubin, C. C. Boutte, The mycobacterial cell envelope — a moving target. *Nature Reviews Microbiology* **18**, 47-59 (2020).
8. S. M. Batt, D. E. Minnikin, G. S. Besra, The thick waxy coat of mycobacteria, a protective layer against antibiotics and the host's immune system. *Biochemical Journal* **477**, 1983-2006 (2020).
9. E. Fullam, R. J. Young, Physicochemical properties and Mycobacterium tuberculosis transporters: keys to efficacious antitubercular drugs? *RSC Medicinal Chemistry* **12**, 43-56 (2021).
10. K. A. Sacksteder, M. Protopopova, C. E. Barry, 3rd, K. Andries, C. A. Nacy, Discovery and development of SQ109: a new antitubercular drug with a novel mechanism of action. *Future Microbiol* **7**, 823-837 (2012).
11. Y.-M. Boudehen *et al.*, Mycobacterial resistance to zinc poisoning requires assembly of P-ATPase-containing membrane metal efflux platforms. *Nature Communications* **13**, 4731 (2022).
12. J. M. Hayashi *et al.*, Spatially distinct and metabolically active membrane domain in mycobacteria. *Proc Natl Acad Sci U S A* **113**, 5400-5405 (2016).
13. R. Bansal-Mutalik, H. Nikaido, Mycobacterial outer membrane is a lipid bilayer and the inner membrane is unusually rich in diacyl phosphatidylinositol dimannosides. *Proceedings of the National Academy of Sciences* **111**, 4958-4963 (2014).
14. M. Gilleron, V. F. J. Quesniaux, G. Puzo, Acylation State of the Phosphatidylinositol Hexamannosides from *Mycobacterium bovis* Bacillus Calmette Guérin and *Mycobacterium tuberculosis* H37Rv and Its Implication in Toll-like Receptor Response *Journal of Biological Chemistry* **278**, 29880-29889 (2003).
15. M. Gilleron *et al.*, Acylation State of the Phosphatidylinositol Mannosides from Mycobacterium bovis Bacillus Calmette Guérin and Ability to Induce Granuloma and Recruit Natural Killer T Cells. *Journal of Biological Chemistry* **276**, 34896-34904 (2001).
16. M. Daffé, H. Marrakchi, Unraveling the Structure of the Mycobacterial Envelope. *Microbiol Spectr* **7** (2019).
17. M. Jackson, The mycobacterial cell envelope-lipids. *Cold Spring Harb Perspect Med* **4**, a021105 (2014).
18. R. Kalscheuer *et al.*, The Mycobacterium tuberculosis capsule: a cell structure with key implications in pathogenesis. *Biochemical Journal* **476**, 1995-2016 (2019).
19. M. E. Guerin, J. Korduláková, P. M. Alzari, P. J. Brennan, M. Jackson, Molecular Basis of Phosphatidyl-*myo*-inositol Mannoside Biosynthesis and Regulation in Mycobacteria *Journal of Biological Chemistry* **285**, 33577-33583 (2010).

20. V. Corradi *et al.*, Emerging Diversity in Lipid–Protein Interactions. *Chemical Reviews* **119**, 5775-5848 (2019).
21. R. A. Corey *et al.*, Identification and assessment of cardiolipin interactions with E. coli inner membrane proteins. *Sci Adv* **7** (2021).
22. H. I. Ingólfsson *et al.*, Lipid Organization of the Plasma Membrane. *Journal of the American Chemical Society* **136**, 14554-14559 (2014).
23. I. D. Pogozheva *et al.*, Comparative Molecular Dynamics Simulation Studies of Realistic Eukaryotic, Prokaryotic, and Archaeal Membranes. *Journal of Chemical Information and Modeling* **62**, 1036-1051 (2022).
24. P. Adhyapak *et al.*, Lipid Clustering in Mycobacterial Cell Envelope Layers Governs Spatially Resolved Solvation Dynamics. *Chemistry – An Asian Journal* **17**, e202200146 (2022).
25. H. Guo *et al.*, Structure of mycobacterial ATP synthase bound to the tuberculosis drug bedaquiline. *Nature* **589**, 143-147 (2021).
26. P. C. T. Souza *et al.*, Martini 3: a general purpose force field for coarse-grained molecular dynamics. *Nature Methods* **18**, 382-388 (2021).
27. R. Alessandri *et al.*, Martini 3 Coarse-Grained Force Field: Small Molecules. *Advanced Theory and Simulations* **5**, 2100391 (2022).
28. L. Borges-Araújo, P. C. T. Souza, F. Fernandes, M. N. Melo, Improved Parameterization of Phosphatidylinositide Lipid Headgroups for the Martini 3 Coarse-Grain Force Field. *Journal of Chemical Theory and Computation* **18**, 357-373 (2022).
29. P. Banerjee, R. Lipowsky, M. Santer, Coarse-Grained Molecular Model for the Glycosylphosphatidylinositol Anchor with and without Protein. *Journal of Chemical Theory and Computation* **16**, 3889-3903 (2020).
30. T. A. Wassenaar, H. I. Ingólfsson, R. A. Böckmann, D. P. Tieleman, S. J. Marrink, Computational Lipidomics with insane: A Versatile Tool for Generating Custom Membranes for Molecular Simulations. *Journal of Chemical Theory and Computation* **11**, 2144-2155 (2015).
31. G. Bussi, D. Donadio, M. Parrinello, Canonical sampling through velocity rescaling. *J Chem Phys* **126**, 014101 (2007).
32. M. Parrinello, A. Rahman, Polymorphic transitions in single crystals: A new molecular dynamics method. **52:12** (1981).
33. M. J. Abraham *et al.*, GROMACS: High performance molecular simulations through multi-level parallelism from laptops to supercomputers. *SoftwareX* **1-2**, 19-25 (2015).
34. J. A. Barker, R. O. Watts, Monte Carlo studies of the dielectric properties of water-like models. *Molecular Physics* **26**, 789-792 (1973).
35. E. L. Wu, Y. Qi, K. C. Song, J. B. Klauda, W. Im, Preferred Orientations of Phosphoinositides in Bilayers and Their Implications in Protein Recognition Mechanisms. *The Journal of Physical Chemistry B* **118**, 4315-4325 (2014).
36. J. Lee *et al.*, CHARMM-GUI Membrane Builder for Complex Biological Membrane Simulations with Glycolipids and Lipoglycans. *Journal of Chemical Theory and Computation* **15**, 775-786 (2019).
37. K. Vanommeslaeghe *et al.*, CHARMM general force field: A force field for drug-like molecules compatible with the CHARMM all-atom additive biological force fields. *Journal of computational chemistry* **31**, 671-690 (2010).
38. J. Huang *et al.*, CHARMM36m: an improved force field for folded and intrinsically disordered proteins. *Nature Methods* **14**, 71-73 (2017).

39. E. L. Wu *et al.*, CHARMM-GUI Membrane Builder toward realistic biological membrane simulations. *Journal of Computational Chemistry* **35**, 1997-2004 (2014).
40. U. Essmann *et al.*, A smooth particle mesh Ewald method. *The Journal of Chemical Physics* **103**, 8577-8593 (1995).
41. S.-J. Marrink (2022) Downloads: Lipids.
42. B. M. Groenewald W, Croft A, Marrink S-J., Molecular Dynamics of Mycolic Acid Monolayers. *ChemRxiv* (2019).
43. P. W. Fowler *et al.*, Membrane stiffness is modified by integral membrane proteins. *Soft Matter* **12**, 7792-7803 (2016).
44. P. Smith, C. D. Lorenz, LiPyphilic: A Python Toolkit for the Analysis of Lipid Membrane Simulations. *Journal of Chemical Theory and Computation* **17**, 5907-5919 (2021).
45. M. Bonomi *et al.*, Promoting transparency and reproducibility in enhanced molecular simulations. *Nature Methods* **16**, 670-673 (2019).
46. S. Buchoux, FATSLiM: a fast and robust software to analyze MD simulations of membranes. *Bioinformatics* **33**, 133-134 (2017).
47. J. D. Hunter, Matplotlib: A 2D Graphics Environment. *Computing in Science & Engineering* **9**, 90-95 (2007).
48. C. UniProt, UniProt: the universal protein knowledgebase in 2021. *Nucleic Acids Res* **49**, D480-D489 (2021).
49. J. Jumper *et al.*, Highly accurate protein structure prediction with AlphaFold. *Nature* **596**, 583-589 (2021).
50. T. Nugent, D. T. Jones, Membrane protein orientation and refinement using a knowledge-based statistical potential. *BMC Bioinformatics* **14**, 276 (2013).
51. P. C. Kroon (2020) Aggregate, automate, assemble. . (University of Groningen), pp 16-53.
52. J. A. Graham, J. W. Essex, S. Khalid, PyCGTOOL: Automated Generation of Coarse-Grained Molecular Dynamics Models from Atomistic Trajectories. *Journal of Chemical Information and Modeling* **57**, 650-656 (2017).
53. S. Kim *et al.*, CHARMM-GUI ligand reader and modeler for CHARMM force field generation of small molecules. *Journal of Computational Chemistry* **38**, 1879-1886 (2017).
54. N. C. f. B. Information (2022) PubChem Compound Summary for CID 5388906, Bedaquiline. (National Center for Biotechnology Information).
55. I. V. Tetko *et al.*, Virtual Computational Chemistry Laboratory – Design and Description. *Journal of Computer-Aided Molecular Design* **19**, 453-463 (2005).
56. A. Waterhouse *et al.*, SWISS-MODEL: homology modelling of protein structures and complexes. *Nucleic Acids Research* **46**, W296-W303 (2018).
57. F. Sievers *et al.*, Fast, scalable generation of high-quality protein multiple sequence alignments using Clustal Omega. *Molecular Systems Biology* **7**, 539 (2011).
58. W. Song *et al.*, PyLipID: A Python Package for Analysis of Protein–Lipid Interactions from Molecular Dynamics Simulations. *Journal of Chemical Theory and Computation* **18**, 1188-1201 (2022).
59. R. A. Corey, O. N. Vickery, M. S. P. Sansom, P. J. Stansfeld, Insights into Membrane Protein–Lipid Interactions from Free Energy Calculations. *Journal of Chemical Theory and Computation* **15**, 5727-5736 (2019).

60. M. Souaille, B. t. Roux, Extension to the weighted histogram analysis method: combining umbrella sampling with free energy calculations. *Computer Physics Communications* **135**, 40-57 (2001).
61. J. S. Hub, B. L. de Groot, D. van der Spoel, g_wham—A Free Weighted Histogram Analysis Implementation Including Robust Error and Autocorrelation Estimates. *Journal of Chemical Theory and Computation* **6**, 3713-3720 (2010).
62. P. S. Schmalhorst, F. Deluweit, R. Scherrers, C.-P. Heisenberg, M. Sikora, Overcoming the Limitations of the MARTINI Force Field in Simulations of Polysaccharides. *Journal of Chemical Theory and Computation* **13**, 5039-5053 (2017).
63. C. Hoffmann, A. Leis, M. Niederweis, J. M. Plitzko, H. Engelhardt, Disclosure of the mycobacterial outer membrane: Cryo-electron tomography and vitreous sections reveal the lipid bilayer structure. *Proceedings of the National Academy of Sciences* **105**, 3963-3967 (2008).
64. B. Zuber *et al.*, Direct visualization of the outer membrane of mycobacteria and corynebacteria in their native state. *J Bacteriol* **190**, 5672-5680 (2008).
65. P. Adhyapak *et al.*, Dynamical Organization of Compositionally Distinct Inner and Outer Membrane Lipids of Mycobacteria. *Biophysical Journal* **118**, 1279-1291 (2020).
66. A. V. Hughes *et al.*, Physical Properties of Bacterial Outer Membrane Models: Neutron Reflectometry & Molecular Simulation. *Biophysical Journal* **116**, 1095-1104 (2019).
67. R. Friedman, Membrane-Ion Interactions. *The Journal of membrane biology* **251**, 453-460 (2018).
68. B. Modak, S. Girkar, R. Narayan, S. Kapoor, Mycobacterial Membranes as Actionable Targets for Lipid-Centric Therapy in Tuberculosis. *Journal of Medicinal Chemistry* **65**, 3046-3065 (2022).
69. P. P. Nguyen, T. Kado, M. Prithviraj, M. S. Siegrist, Y. S. Morita, Inositol acylation of phosphatidylinositol mannosides: a rapid mass response to membrane fluidization in mycobacteria. *Journal of Lipid Research* **63** (2022).
70. J. H. Lorent *et al.*, Plasma membranes are asymmetric in lipid unsaturation, packing and protein shape. *Nat Chem Biol* **16**, 644-652 (2020).
71. G. von Heijne, Net N-C charge imbalance may be important for signal sequence function in bacteria. *Journal of Molecular Biology* **192**, 287-290 (1986).
72. J. A. Baker, W.-C. Wong, B. Eisenhaber, J. Warwicker, F. Eisenhaber, Charged residues next to transmembrane regions revisited: "Positive-inside rule" is complemented by the "negative inside depletion/outside enrichment rule". *BMC Biology* **15**, 66 (2017).
73. I. D. Pogozheva, S. Tristram-Nagle, H. I. Mosberg, A. L. Lomize, Structural adaptations of proteins to different biological membranes. *Biochimica et Biophysica Acta (BBA) - Biomembranes* **1828**, 2592-2608 (2013).
74. R. J. Anderson, P. W. Groundwater, A. Todd, A. J. Worsley, *Antibacterial agents : chemistry, mode of action, mechanisms of resistance and clinical applications* (Wiley-Blackwell, Chichester, 2012), pp. 378.
75. V. A. Dartois, E. J. Rubin, Anti-tuberculosis treatment strategies and drug development: challenges and priorities. *Nature Reviews Microbiology* 10.1038/s41579-022-00731-y (2022).
76. A. Krah, G. Grüber, P. J. Bond, Binding properties of the anti-TB drugs bedaquiline and TBAJ-876 to a mycobacterial F-ATP synthase. *Current Research in Structural Biology* **4**, 278-284 (2022).

77. F. Bardou, C. Raynaud, C. Ramos, M. A. Lanéelle, G. Lanéelle, Mechanism of isoniazid uptake in Mycobacterium tuberculosis. *Microbiology* **144**, 2539-2544 (1998).
78. A. N. Unissa, S. Subbian, L. E. Hanna, N. Selvakumar, Overview on mechanisms of isoniazid action and resistance in Mycobacterium tuberculosis. *Infection, Genetics and Evolution* **45**, 474-492 (2016).
79. M. Jackson *et al.*, Inactivation of the antigen 85C gene profoundly affects the mycolate content and alters the permeability of the Mycobacterium tuberculosis cell envelope. *Molecular Microbiology* **31**, 1573-1587 (1999).
80. A. L. Duncan, A. J. Robinson, J. E. Walker, Cardiolipin binds selectively but transiently to conserved lysine residues in the rotor of metazoan ATP synthases. *Proceedings of the National Academy of Sciences* **113**, 8687-8692 (2016).
81. R. A. Corey, P. J. Stansfeld, M. S. P. Sansom, The energetics of protein-lipid interactions as viewed by molecular simulations. *Biochem Soc Trans* **48**, 25-37 (2020).
82. J. Briffotaux, W. Huang, X. Wang, B. Gicquel, MmpS5/MmpL5 as an efflux pump in Mycobacterium species. *Tuberculosis* **107**, 13-19 (2017).
83. G. Degiacomi *et al.*, In vitro Study of Bedaquiline Resistance in Mycobacterium tuberculosis Multi-Drug Resistant Clinical Isolates. *Frontiers in Microbiology* **11** (2020).
84. R. J. Clarke, K. R. Hossain, K. Cao, Physiological roles of transverse lipid asymmetry of animal membranes. *Biochimica et Biophysica Acta (BBA) - Biomembranes* **1862**, 183382 (2020).
85. W. Im, S. Khalid, Molecular Simulations of Gram-Negative Bacterial Membranes Come of Age. *Annual Review of Physical Chemistry* **71**, 171-188 (2020).
86. J. Augenstreich *et al.*, The conical shape of DIM lipids promotes *Mycobacterium tuberculosis* infection of macrophages. *Proceedings of the National Academy of Sciences* **116**, 25649-25658 (2019).
87. A. Queiroz, L. W. Riley, Bacterial immunostat: Mycobacterium tuberculosis lipids and their role in the host immune response. *Rev Soc Bras Med Trop* **50**, 9-18 (2017).
88. K. A. Abrahams, G. S. Besra, Synthesis and recycling of the mycobacterial cell envelope. *Current Opinion in Microbiology* **60**, 58-65 (2021).